Why $Ti_3C_2T_x$ MXenes Are Conductive but Not Plasmonic in the Optical Domain

Hui Fang,[1,6] Zhenyao Fang,[1,6] Anupma Thakur,[2,6] Vahid Rad,[3]
Nithin Chandran B.S.,[2] Paweł P. Michałowski,[4] Masoud Soroush,[3]
Babak Anasori,[2,5*] Andrew M. Rappe,[1*] Zahra Fakhraai[1*]

[1]Department of Chemistry, University of Pennsylvania, Philadelphia, PA 19104, USA
[2]School of Materials Engineering, Purdue University, West Lafayette, IN 47907, USA
[3]Department of Chemical and Biological Engineering, Drexel University, Philadelphia, PA 19104, USA
[4]Łukasiewicz Research Network—Institute of Microelectronics and Photonics, Warsaw, Poland
[5] School of Mechanical Engineering, Purdue University, West Lafayette, IN 47907, USA
[6]Contributed equally to this work

*To whom correspondence should be addressed; E-mail: banasori@purdue.edu;
rappe@sas.upenn.edu; fakhraai@sas.upenn.edu.

MXenes have shown great potential in electronic and optoelectronic applications. However, optical properties of these highly conductive two-dimentional materials are not fully understood. The near-infrared (IR) optical peak (∼1.5 eV) in $Ti_3C_2T_x$ with mixed terminations (T: =O, −OH, −F, −Cl) has sparked debates, attributing the peak to a localized surface plasmon resonance (LSPR) or an inter-band transition (IBT). Here, density functional theory calculations conclusively assign the peak to an IBT that exists only in $Ti_3C_2O_2$. Both experiments and calculations corroborate that this peak is absent in $Ti_3C_2Cl_2$. Moreover, calculations predict SPR in the mid-IR (∼0.5 eV, outside optical domain) for $Ti_3C_2O_2$, but not for $Ti_3C_2Cl_2$. Our results reconcile conflicting in-

terpretations of the debate, allowing for optimized use of $Ti_3C_2T_x$ MXenes, by leveraging their IBT optical signature, which is size-independent and distinct from the size-dependent plasmonic effect.

INTRODUCTION

As a new family of two-dimensional (2D) materials discovered in 2011 (*1*), MXenes have attracted great interest for various electronic and optoelectronic applications (*2–4*), as they possess outstanding electronic, optical, and mechanical properties (*2, 5, 6*). MXenes have the general chemical formula of $M_{n+1}X_nT_x$ ($n = 1 - 4$), where M represents a transition metal, X carbon and/or nitrogen, and T_x surface terminations (–F, –Cl, =O, –OH) (*2*). Their diversity in surface termination, ease of functionalization, and stoichiometric composition results in various tunable properties, broadening the range of their potential applications (*7–11*).

MXenes have been demonstrated to have high free-carrier density (*12*) as well as tunable optical properties (*3, 13*), making them excellent candidates for optoelectronic devices (*2, 14*). The extensively studied MXene $Ti_3C_2T_x$ exhibits intense free-carrier absorption from the near- to mid-infrared (IR) (*15*). Notably, a distinct near-IR absorption peak at around 800 nm (≈1.5 eV) has been widely reported for $Ti_3C_2T_x$ (*13, 16*). However, the assignment of this absorption peak is still under debate. Two possible origins have been proposed: inter-band transition (IBT) or localized surface plasmon resonance (LSPR) (*13, 17*). Density-functional theory (DFT) calculations demonstrated that this peak is an optically active IBT (*18, 19*), which can vary with the surface termination type. This was indirectly corroborated by our previous work (*16*), which showed that this peak lacked strong anisotropic properties, typically seen in anisotropic plasmonic nanomaterials (*20–22*). Further evidence supporting the IBT hypothesis includes the observation that this peak is independent of lateral size (*23*) and solvent type (*24*) in UV-Vis spectroscopy measurements.

Scanning transmission electron microscopy (STEM)-electron energy loss spectroscopy (EELS) measurements indicate the presence of a transverse SPR (surface plasmon resonance) owing to the uniform distribution of the resonance over the entire area of a flake (*25*). This observation has been taken as evidence of the existence of localized or bulk plasmon resonances around 1.5 eV. Ultrafast transmittance and reflectance studies supported this plasmonic behavior by comparing the transient response of the 1.5 eV peak, which differs significantly from that of IBT (*26*). Additional evidence supporting the plasmonic hypothesis was provided in the blue-shift of the peak energy, observed when MXene films were used as cathodes in electrochromic devices. This shift was attributed to a plasmon influenced by a voltage-driven increase in the electron density (*27*). A similar blue-shift with increasing carrier concentration has also been confirmed by comparing different batches of $Ti_3C_2T_x$ MXenes with variations in synthesis and processing (*13*). Additionally, multi-photon photoemission electron microscopy (nP-PEEM) experiments revealed a dispersive surface plasmon polariton between 1.4 and 1.9 eV on $Ti_3C_2T_x$ MXene flakes (*28*). Other EELS results, however, place the location of the SPR in the IR region with energy at 0.6–0.9 eV or 0.3 eV (*15, 29*). Adding to the debate, most recent studies have shown that this 1.5 eV optical peak may have a dual origin, stemming from both inter-band transitions and plasmonic effects, as evidenced by DFT calculations and ellipsometry measurements (*30, 31*). These contradictory reports raise questions regarding the nature of $Ti_3C_2T_x$ interactions with photons.

In this work, we resolve this debate by investigating the properties of the near-IR absorption peak of $Ti_3C_2T_x$ with mixed terminations (T representing the mixture of $=$O, $-$OH, $-$Cl, and $-$F), and that of $Ti_3C_2Cl_2$ with predominantly $-$Cl terminations . Through DFT calculations, we demonstrate that the typically measured near-IR absorption band at 1.5 eV in $Ti_3C_2T_x$ originates from a low-energy IBT due to its oxygen terminations ($=$O). Using spectroscopic ellipsometry (SE) and other experimental measurements, we show that this extinction peak nearly vanishes

in $Ti_3C_2Cl_2$ MXenes, which are free of oxygen terminal groups. We also explore the effects of film thickness and intercalated inter-flake water on the properties of this IBT. Moreover, we calculate the dispersion relation of propagating surface plasmons in monoflakes and show that the effect can strongly depend on the surface termination. Only $Ti_3C_2O_2$ MXenes show a strong SPR, which is located at 0.5 eV, well-separated from the IBT at 1.5 eV. Propagating or localized SPR (LSPR) are absent or strongly attenuated in $Ti_3C_2Cl_2$ and other simulated MXenes. The experimental data corroborates that while propagating surface plasmons may be sustained, resonance features are absent in both $Ti_3C_2T_x$ and $Ti_3C_2Cl_2$ MXenes in the measured spectral window of 0.73–3.34 eV, as these waves are strongly attenuated due to the strong dielectric loss. As such, it is also unlikely that LSPR can be sustained in these MXenes. Our results reconcile the previous debates on the existence and location of SPR in $Ti_3C_2T_x$ MXenes, and they shed light on the origins of the optical properties of $Ti_3C_2T_x$ MXenes, opening avenues for further exploration in electronic and optoelectronic applications.

RESULTS

$Ti_3C_2T_x$ with mixed surface terminations and $Ti_3C_2Cl_2$ with $-$Cl terminations MXenes were chosen for this work. The synthesis and characterization details of these MXenes are described in the Materials and Methods section, Supplementary Note S1, and Figs. S1-S6. The atomic percentages of oxygen and chlorine were determined by X-ray photoelectron spectroscopy (XPS) survey spectra (Fig. S4, Table S1) to be 20.89% and 2.33%, respectively, for $Ti_3C_2T_x$; and 6.51% and 26.19%, respectively, for $Ti_3C_2Cl_2$. This indicates that the O-containing terminal groups dominate in the $Ti_3C_2T_x$ while Cl terminations dominate in $Ti_3C_2Cl_2$, consistent with previous results (*32, 33*). This observation is also consistent with the energy dispersive spectroscopy (EDS) results (Fig. S5, Table S2). However, the absence of oxygen in $Ti_3C_2Cl_2$ (Fig. S6, Table S3) was confirmed by secondary ion mass spectrometry (SIMS) with atomic depth

resolution (*34,35*), which was used to determine the elemental composition of each atomic layer. The average concentration of =O, −OH, −F, and −Cl species in $Ti_3C_2T_x$ termination layer is 43.1%, 25%, 27.8%, and 4.2%, respectively—comparable with the XPS and EDS results. This slight discrepancy in the O content observed from XPS and EDS ($< 7\%$) measurements and from SIMS (0%), might result from variations in the measurement depths of these techniques and differences in sample preparation. Both XPS and EDS are surface sensitive, so the detected oxygen could originate from adsorbed oxygen on the surface or potential edge oxidation during the post-processing of MXenes after synthesis; meanwhile, SIMS measures the bulk region (at least 250 nm below the surface in our case). Edge oxidation for $Ti_3C_2T_x$ has been discussed in our previous work (*36*), and the investigation for $Ti_3C_2Cl_2$ will be discussed in future works.

To determine the optical properties of these MXenes, variable-angle SE measurements were performed on both monoflake ($\sim$1 nm) and multiflake ($\sim$60 nm) films at room temperature (Figures S7-S8) (*16*). The SE fitting is detailed in the Supplementary Note S2 and Tables S4-5. The results for $Ti_3C_2T_x$ are comparable with previously reported SE measurements (*16, 26, 37–39*).

Near-IR absorption peak is an inter-band transition made possible by oxygen termination

The extinction coefficients (k) of as-prepared $Ti_3C_2T_x$ and $Ti_3C_2Cl_2$ MXene monoflake films, extracted from the SE fitting, are presented in Fig. 1A. Similar results for multiflake films ($\sim$60 nm) are shown in Fig. S8F. The increasing extinction as the energy decreases below 1 eV, seen in Fig. 1A for both MXenes, is due to the free-carrier absorption. This portion of the spectrum can be fitted by a Drude function to extract the respective resistivity or conductivity of $Ti_3C_2T_x$ and $Ti_3C_2Cl_2$ MXenes, similar to previous reports for $Ti_3C_2T_x$ (*13, 16*). The resistivity of $Ti_3C_2Cl_2$ ($(1.8 \pm 0.1) \times 10^{-3}$ Ohm·cm for monoflake and $(1.8 \pm 0.1) \times 10^{-3}$ Ohm·cm for

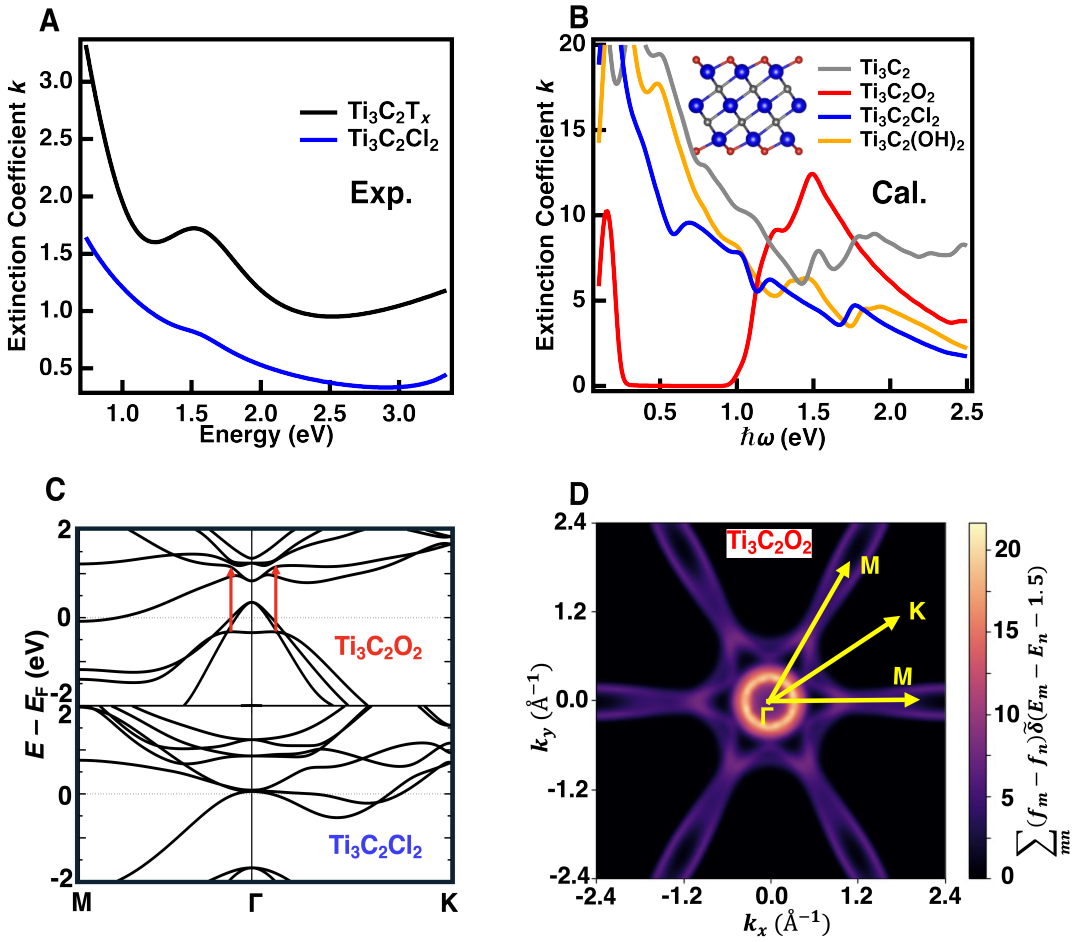

Fig. 1. Optical properties of $Ti_3C_2T_x$ and $Ti_3C_2Cl_2$ MXenes. (A) The measured extinction coefficient (k) of as-prepared $Ti_3C_2T_x$ (black curve) and $Ti_3C_2Cl_2$ (blue curve) MXene monoflake films with similar thicknesses ($\sim$1 nm) extracted from the SE measurements shown in Figure S6 (SI). (B) Calculated k of bare Ti_3C_2, $Ti_3C_2O_2$, $Ti_3C_2Cl_2$, and $Ti_3C_2(OH)_2$ monoflakes with a smearing width of 0.05 eV. The inset shows the unit cell used for $Ti_3C_2O_2$. Color code: Ti (blue), C (grey), O (red). (C) The calculated electronic structures of $Ti_3C_2O_2$ (top) and $Ti_3C_2Cl_2$ (bottom) monoflakes along the high-symmetry lines, where the red arrows indicate the optical transitions contributing to the 1.5-eV peak in the extinction coefficient. (D) The reciprocal-space-resolved contribution from the energy-matching criteria to the 1.5-eV peak in the extinction coefficient spectrum of the $Ti_3C_2O_2$ monoflake. The arrows show the directions in a Brillouin zone.

multiflake films) is higher than that of $Ti_3C_2T_x$ ($(0.5 \pm 0.1) \times 10^{-3}$ Ohm·cm for monoflake and $(1.0 \pm 0.1) \times 10^{-3}$ Ohm·cm for multiflake films), which is in line with the electrical resistivity trend (Table S6) measured by four-point probe methods. This difference is attributed to the differences in synthesis and delamination protocols, surface termination groups, and potentially larger number of defects in $Ti_3C_2Cl_2$, as the flake sizes in these MXenes are on average smaller than $Ti_3C_2T_x$ (Figs. S2-S3), which has been extensively optimized to have lower defects and higher conductivity (*40*).

In addition to the Drude conductivity, two distinct extinction peaks are observed in both MXenes, which were fitted to harmonic oscillators (Tables S4-S5): Harmonic 1 at 1.5 eV and Harmonic 2 at 3.6 eV. The peak at 3.6 eV has been unambiguously attributed to an IBT (*18*). The near-IR extinction peak (Harmonic 1) was attributed to an LSPR in $Ti_3C_2T_x$ (*25*), a widely held belief within the community. However, our recent results (*16*) indicated that the optical details of this oscillator are not consistent with LSPR, which are often strongly anisotropic in non-isotropic plasmonic particles (*20*). As shown in Fig. 1A, this peak is dramatically suppressed in $Ti_3C_2Cl_2$, where the surface terminations are predominantly $-$Cl, compared to that of $Ti_3C_2T_x$ with mixed terminations, which are predominantly $=$O groups (*2*). UV-Vis spectra measured for $Ti_3C_2T_x$ and $Ti_3C_2Cl_2$ colloidal solutions in DMSO (dimethylsulfoxide) also show dramatically suppressed extinction in the near-IR spectral region (Fig. S9), similar to a previous report (*41*). Both the SE and UV-Vis results indicate that the surface terminations play a significant role in the origin of this extinction peak.

To explore the effects of the surface terminations on this near-IR extinction peak, the extinction coefficients of monoflakes of singly terminated $Ti_3C_2T_2$ MXene with $=$O, $-$F, $-$OH, $-$H, $-$Cl, and bare terminations were calculated using DFT. As shown in Table S7, MXenes with $-$F, $=$O, $-$OH, and $-$Cl terminations are more stable than the bare MXene, while the H-terminated MXene is thermodynamically less stable and is thus unlikely to be observed experimentally.

This is consistent with previous reports (*36, 42*). The optical extinction of MXenes with −Cl, =O, −OH, and bare terminations, calculated with a smearing width of 0.05 eV, is shown in Fig. 1B. The results for all terminations and the corresponding optical conductivities with different smearing widths are in the Fig. S10. The band structures for $Ti_3C_2O_2$ and $Ti_3C_2Cl_2$ are shown in Fig. 1C, and those for all singly terminated $Ti_3C_2T_2$ are in the SI (Fig. S11). It is noted that the smearing width of 0.5 eV generates spectra that are similar to the experimental spectra (Fig. S10) but miss key physical details. As such, the smearing width of 0.05 eV was selected for this study. Detailed discussions on the choices of the smearing width are in Supplementary Note S4.

As seen in the band structure (Figs. 1C, S11) and the extinction coefficient results (Figs. 1B,S10), all monoflake MXenes, regardless of their termination, are conductive and show an increasing extinction coefficient at low energy. By comparing the calculated extinction coefficients of the MXenes singly terminated with −Cl, =O, and −OH (Fig. 1B)—the three most stable terminations, which are also the terminations typically observed in experiments (*36, 40*)—we can see that the O-terminated monoflake ($Ti_3C_2O_2$) has a markedly different extinction spectral feature. An additional extinction feature at around 1.5 eV is observed for this $Ti_3C_2O_2$ MXene, which is absent for $Ti_3C_2Cl_2$ and $Ti_3C_2(OH)_2$ MXenes; this is even more clear in calculations with a larger smearing width of 0.5 eV (Fig. S10). This suggests that this near-IR extinction peak is from the =O terminations of MXenes. This matches well with the experimental observation shown in Fig. 1A, where the 1.5 eV peak is nearly fully attenuated in the $Ti_3C_2Cl_2$ MXene (predominantly −Cl) while it is prominently present in $Ti_3C_2T_x$ (predominantly terminated by O-containing groups; based on the calculations, most likely =O). The tiny 1.5 eV peak in $Ti_3C_2Cl_2$ (Fig. 1A) can be attributed to the surface absorbed oxygen or potential edge oxidation due to post-processing, as XPS and EDS identified a small ($< 7\%$) oxygen content in these MXenes (Figs. S4-S5). However, this oxygen is not directly associated with =O terminations

introduced during the synthesis process, as evidenced by the SIMS results (Fig. S6).

In order to explore the origin of this near-IR peak, the optical conductivity of $Ti_3C_2O_2$ MXene (Equation 2) was split into the $\mathbf{k}$-dependent optical transition magnitude $v^{\alpha}_{mn}(\mathbf{k})v^{\beta}_{nm}(\mathbf{k})$ and the smeared δ-function $(f_{n\mathbf{k}} - f_{m\mathbf{k}})\tilde{\delta}(\hbar\omega - (E_{n\mathbf{k}} - E_{m\mathbf{k}}))$, which requires that the energy difference between the two bands involved in the optical transitions is close to the input photon energy, where the $\hbar\omega = 1.5$ eV was fixed, and $\tilde{\delta}(E)$ represents the smeared normal distribution. The calculated $\mathbf{k}$-resolved smeared normal function (weighted by the Fermi–Dirac occupation) is shown in Fig. 1D. It is clear that the transitions involving the electronic states near the Γ point contribute more to this term and further to the peak at 1.5 eV in the optical conductivity and extinction coefficient spectrum. As shown in Fig. 1C (top), the conduction bands and the valence bands near the Brillouin zone center exhibit a "nearly flat band" behavior for $Ti_3C_2O_2$, with an energy difference close to 1.5 eV. These nearly flat bands are absent for $Ti_3C_2Cl_2$ (Fig. 1C, bottom) and the $Ti_3C_2T_2$ MXenes with the other considered surface terminations (SI: Fig. S11), justifying that only the O-terminated monoflake has this IBT in its extinction coefficient spectrum. The location of this IBT is also consistent with previous DFT calculations (*19, 43*).

Effect of the inter-band transition on propagating surface plasmons

To further investigate the surface plasmon effect, the dispersion relation of the surface plasmon mode of $Ti_3C_2T_x$ and of $Ti_3C_2Cl_2$ monoflake films in vacuum was calculated based on Equation 8. The calculations were performed based on the experimentally measured dielectric constant of monoflake films shown in Figs. 2A,B. An SPR on the film surface is expected when the real part of the dielectric constant $\varepsilon_1 = -1$ (surface wave energy, $E_{\mathrm{s}} \approx 1.0$ eV for $Ti_3C_2T_x$; $E_{\mathrm{s}} < 1.0$ eV for $Ti_3C_2Cl_2$, dashed line in Fig. 2A). The calculated plasmon dispersion relations are shown in Figs. 2C,D. As seen in this figure, a clear SPR feature is missing at the expected SPR energy of $E_s \approx 1.0$ eV for $Ti_3C_2T_x$ where the resonance criteria are expected. Similar results

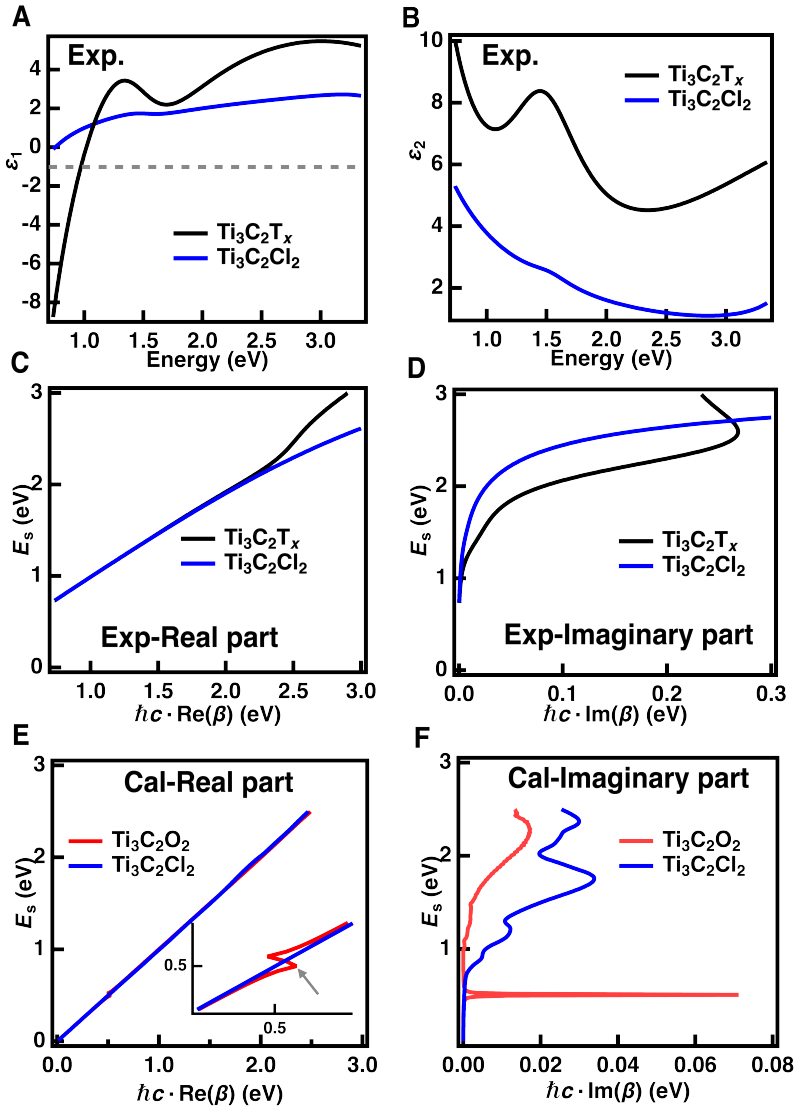

Fig. 2. Surface plasmon dispersion for monoflake MXenes with different surface terminations. (A) Real (ε_1) and (B) imaginary (ε_2) parts of the dielectric constant as a function of energy for MXene monoflakes, $Ti_3C_2T_x$ (black) and $Ti_3C_2Cl_2$ (blue), extracted from the SE fitting in Fig. S7. (C) Real and (D) imaginary part of the dispersion relation of surface plasmon waves for MXene monoflakes in vacuum, calculated based on the experimentally measured dielectric constants shown in (A) and (B). (E, F) The corresponding dispersion curves, calculated based on the dielectric constants of $Ti_3C_2O_2$ (red) and $Ti_3C_2Cl_2$ (blue) monoflakes. The inset in (C) shows a zoomed-in version of the curve around the SPR in $Ti_3C_2O_2$, where the gray arrow indicates the energy of the propagating surface plasmon waves. In all curves, E_s is the surface wave energy, β is the in-plane wavevector, $\hbar$ is the reduced Planck constant, and c is the speed of light.

are observed for multiflake films (Fig. S12), where the E_s values (when $\varepsilon_1 = -1$) shift to higher energy but still less than 1.5 eV.

The plasmon dispersions of simulated $Ti_3C_2O_2$ and $Ti_3C_2Cl_2$ MXenes were also calculated from the total dielectric function using a similar approach (details inMaterials and Methods). As shown in Figs. 2E,F, a characteristic frequency for SPR is observed around 0.5 eV (just outside the experimental window) in $Ti_3C_2O_2$ MXenes. This resonance is absent in Cl-terminated and F-terminated MXenes (Fig. S13). The 0.5 eV SPR is consistent with the previous EELS measurements as well as the previous *ab initio* theoretical calculations (*15*).

It is important to note that while additional spectral features can be seen in the imaginary part of the dispersion relation for both experimental and simulated MXenes (Figs. 2D,F) in the visible spectral window (1–3 eV), neither of these features are well-defined SPR, where a discontinuity, as opposed to small velocity distortions, is expected in the real part of the dispersion relation (*44*). We also note that these features strongly depend on the surface terminations of the MXene and are not in any way correlated with the extinction peak of $Ti_3C_2O_2$ at $\sim$1.5 eV. For example, the termination effect on surface propagation velocity is stronger in $Ti_3C_2Cl_2$ at 1.5 eV than in $Ti_3C_2O_2$ (Fig. 2F), despite the absence of the IBT in this MXene (Fig. 1C, bottom). Similarly, if one were to calculate the SPR based on the dielectric constant of multiflake MXene films, with stronger extinction (Fig. S12), the exact location of the calculated SPR would vary. Regardless, the strong damping of the waves due to dielectric loss in MXenes would still prevent the SPR propagation. As such, the experimentally observed peak at $\sim$1.5 eV is conclusively assigned to the IBT between the nearly flat band states of =O terminations of $Ti_3C_2T_x$ MXenes, while the observed propagating surface plasmon waves in PEEM and EELS experiments (*25, 28*) are unrelated to the presence of the $\sim$1.5 eV IBT.

It is also important to note that while the metallic nature of MXenes with a bulk plasmon frequency of $\omega_p = 6$–7 eV (depending on the termination group) can potentially result in localized

SPR (LSPR), the results in Fig. 2 suggest that strong dielectric loss in MXenes significantly dampens surface plasmon waves, preventing their long-distance propagation. As such, while propagating surface waves may be observed under the strong energy injection in PEEM or EELS experiments (*25, 28*), incoherent optical light is unlikely to result in LSPR, either in the in-plane or out-of-plane directions.

Effect of water on the low-energy inter-band transition

It has been theoretically demonstrated that intercalated water could affect the density of states and chemical properties of $Ti_3C_2O_2$ MXene (*45*). Water can also lead to reduced photostability in $Ti_3C_2T_x$ (*46*), indicating the potential effects of intercalated water on optical properties. It is thus important to explore the role of intercalated water in changes in the optical properties of $Ti_3C_2T_x$, particularly on the low-energy IBT.

Our previous work demonstrated that intercalated water between randomly stacked $Ti_3C_2T_x$ MXene flakes can have a high barrier for removal (*36*). While vacuum annealing above 200 °C can remove bulk-like physisorbed inter-flake water, the complete removal of confined water requires vacuum annealing above 500 °C. For example, 2 hours of vacuum annealing at 600 °C can fully remove both the physisorbed and the confined water and alter the termination states to make MXene surfaces more hydrophobic (*36*). To explore the effects of the intercalated water on optical properties, SE measurements were performed on $Ti_3C_2T_x$ MXene multiflake films after various vacuum annealing protocols (more details in the Materials and Methods). The extracted extinction coefficient results are shown in Fig. 3A; blue-shifting of the near-IR IBT is observed upon the removal of water. The near-IR IBT energy of the as-prepared film with both physisorbed and confined (chemisorbed) water is measured at 1.61 ± 0.26 eV (black curve in Fig. 3A). In comparison, when the physisorbed water is removed by 200 °C vacuum annealing (orange curve), the transition energy blue-shifts to 1.63 ± 0.25 eV. Upon the removal of both

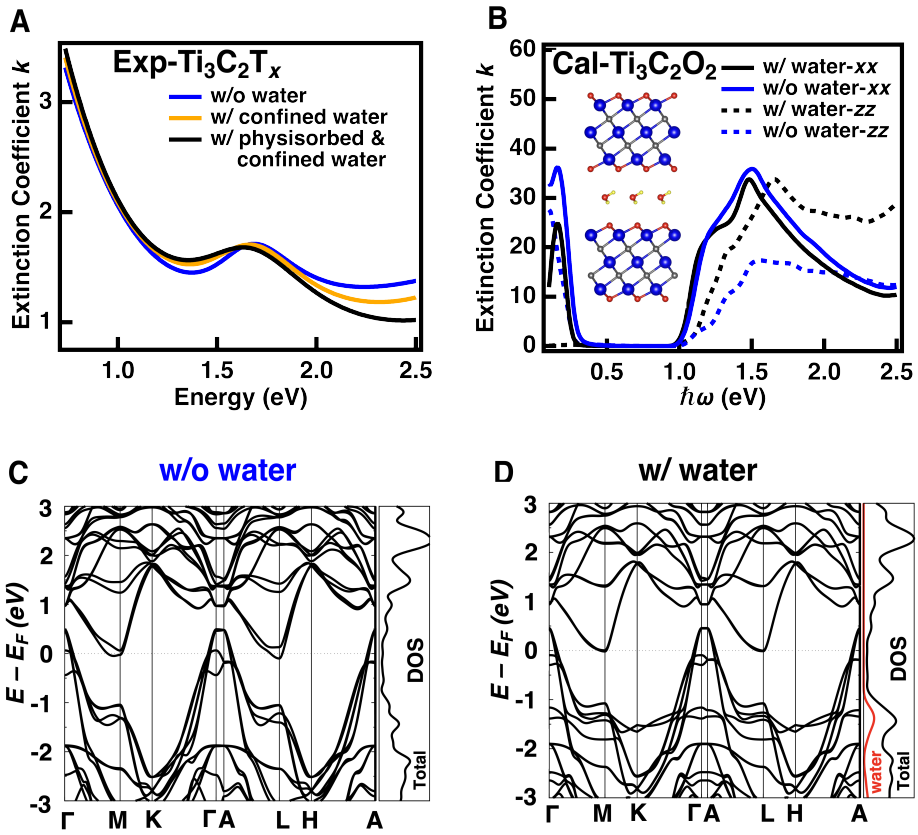

Fig. 3. The effect of intercalated water on bulk optical properties. (A) The measured extinction coefficients of multiflake films at room temperature for an as-prepared film without vacuum-annealing with both physisorbed and confined water (black curve), a film vacuum-annealed at 200 °C for 24 h, where only confined water exists (orange curve), and a film vacuum-annealed at 600 °C for 2 h, where all of the water removed (blue curve). (B) The calculated in-plane (xx, solid curves) and out-of-plane (zz, dashed curves) components of the extinction coefficient of bulk $Ti_3C_2O_2$ without or "w/o" (blue) and with or "w/" (black) intercalated water. (C,D) band structure of bulk $Ti_3C_2O_2$ without and with water. A plot of the density of states (DOS) vs. energy is shown on the right side of both (C) and (D). In (D), the DOS of water is shown in red.

physisorbed and confined water by annealing at more elevated temperatures (i.e., 600 °C), a more significant blue-shift to 1.65 ± 0.22 eV is observed. More averaged results are in the Table S8.

To understand the origins of this blue-shift in the optical spectra, the band structure, optical conductivity, and the extinction coefficient of bulk $Ti_3C_2O_2$ without and with intercalated water molecules were calculated. In these simulations, stacked MXene layers were modeled without water or with an intercalated water monolayer with a zigzag configuration (Fig. S15A). More calculation details and the water configuration effects are discussed in the Supplementary Note S5. The calculated in-plane (xx) and out-of-plane (zz) extinction coefficients of stacked MXene layers (bulk) without and with water monolayers are shown in Fig. 3B, and the corresponding band structures and densities of states are shown in Figs 3C,D. As seen in Fig. 3D, the electronic states of water layers are below the Fermi level by at least 1 eV (Supplementary Note S5), suggesting that the optical conductivity is not significantly affected by the presence of water layers unless the photon energy is greater than 1 eV. This is consistent with the calculated extinction coefficients of bulk $Ti_3C_2O_2$, shown in Fig. 3B, where the overall trends are similar for bulk $Ti_3C_2O_2$ with or without the water monolayers. The effect of water is primarily observed above 1 eV and in the zz-direction, where water facilitates conductivity, increasing the extinction coefficient above 1 eV. Moreover, in the xx-direction, the extinction arising from the IBT at 1.5 eV shifts to higher energy when the intercalated water layer is removed (Fig. 3B, blue curve, solid line), relative to when a water layer is present (Fig. 3B, black curve, solid line). This trend is in line with the experimentally observed blue-shift of this transition upon the complete removal of water (Fig. 3A). Our calculations can also explain the previously observed 1.5 eV blue-shift in $Ti_3C_2T_x$, both during cathodic potential scans in electrochromic devices (*27*) and in samples prepared by different synthesis protocols (*13*), without the presence of a plasmon resonance.

We note that while the calculated extinction coefficients in bulk MXenes with or without

water are anisotropic, the degree of anisotropy is small and is primarily observed at high energy. Although it has been demonstrated that the SE data cannot be reliably fitted to an anisotropic model for heterogeneously stacked MXene films in our previous work (*16*), it is helpful to note that as shown in Fig. 3B, the zz-component always shows higher peak energy than that of the xx-component, whether water is present or not. As such, a small blue-shift would be expected in the isotropic SE extinction spectra of thick films compared to thin films, given that they have a larger number of stacked flakes. Indeed, the SE results with isotropic fitting corroborate this hypothesis (Tables S4-S5). It is observed that the IBT energy shifts from 1.5 to 1.6 eV as the as-prepared $Ti_3C_2T_x$ film thickness increase from $\sim$1 to $\sim$60 nm. In contrast, for the small peak in the spectrum of Ti_3C_2Cl, where fewer =O terminations are present, no significant blue-shift is observed between monoflake ($\sim$1 nm) and multiflake ($\sim$60 nm) films, either due to the reduced number of intercalated water molecules, the reduced contribution of the IBT, or both. An extensive investigation of intercalated water in Ti_3C_2Cl in the future should provide more insight but is outside the scope of this study.

DISCUSSION

In conclusion, our combined use of SE measurements and DFT calculations resolved long-standing debates regarding the origins of the key optical signatures of $Ti_3C_2T_x$ MXenes. We established that the near-IR absorption peak ($\sim$1.5 eV) arises from IBT between nearly flat band states near the Γ point, associated with oxygen (=O) surface terminations, rather than the previously suggested LSPR. This peak is significantly attenuated and is barely measurable in $Ti_3C_2Cl_2$, which might contain minimal oxygen due to surface adsorption or edge oxidation. Our analysis revealed that the dispersion of propagating surface plasmons is highly sensitive to the type of surface terminations; it is only prominently seen in $Ti_3C_2O_2$ at around 0.5 eV, well outside the optical window. Furthermore, we demonstrated that thicker MXene films and the

removal of intercalated water can induce apparent blue-shifts in this IBT due to the influence of water in facilitating out-of-plane conductivity. These findings advance the understanding of optical properties of $Ti_3C_2T_x$, providing a foundation for their future use in electronic and optoelectronic applications.

MATERIALS AND METHODS

Sample Preparation

Synthesis of Ti_3AlC_2 MAX Optimized Ti_3AlC_2 MAX phase was synthesized by combining titanium carbide, titanium, and aluminum in the molar ratio of 2:1.25:2.2 (*47*). Subsequently, the mixture was jar-milled in Nalgene high-density polyethylene bottles along with yttria-stabilized zirconia balls(ball-to-powder mass ratio of 2:1) for 18 hours at 64 revolutions-per-minute (RPM). The jar-milled powders were packed into an alumina crucible, covered with graphite foil, and placed in a high-temperature tube furnace (Carbolite Gero, 1700 °C model) for reactive pressureless sintering. Before starting the heating cycle, the furnace was purged with argon (99.999% purity) for 20 minutes. Subsequently, it was subjected to a controlled heating process, gradually raising the temperature to 1400 °C with a steady heating rate of 3.5 °C/min, and 4 hours dwell, ensuring an uninterrupted flow of argon. Following the 4-hour sintering process, the furnace was gradually cooled down to room temperature at a controlled rate of 10 °C/min. The sintered block was milled into a fine powder (< 71 μm) using a TiN-coated mill bit.

Synthesis of $Ti_3C_2T_x$ MXene The detailed synthesis procedures can be found in our previous work (*40*). Briefly, for optimized $Ti_3C_2T_x$ MXene synthesis, 1 g of Ti_3AlC_2 MAX phase was first washed using 9 M HCl for 18 h to remove the intermetallic impurities and then mixed with an etchant solution (6:3:1 mixture (by volume) of 12 M HCl, DI water, and 50 wt % HF and

stirred at 400 rpm for 24 h at 35 °C. The etched $Ti_3C_2T_x$ MXene was washed with deionized water via repeated centrifugation at 3234 relative centrifugal force (RCF, 4-5 cycles with $\sim$ 200 mL of deionized water) until the supernatant reached pH $\sim$ 6. For delamination, the etched multilayered $Ti_3C_2T_x$ MXene sediment (typically 50 mL/per gram of starting etched powder) was then added to 0.5 M LiCl solution. The mixture of LiCl and etched multilayered $Ti_3C_2T_x$ MXene was then stirred at 400 rpm for 1 h at 65 °C under constant argon flow. The mixture was then washed with deionized water via centrifugation at 3234 RCF for 5, 10, 15, and 20 minutes. The final mixture was then vortexed for 30 minutes followed by centrifugation at 2380 RCF for 30 minutes to ensure the MXene solutions only contained single-to-few-layered flakes. The final suspension of $Ti_3C_2T_x$ MXene was collected and stored in a freezer at -20 °C until use.

Synthesis of $Ti_3C_2Cl_2$ MXene For 1 g of pre-etch acid-washed excess metal-Ti_3AlC_2 MAX powder, $ZnCl_2$ (Thermo Fisher, $>$99%, anhydrous) was used as the Lewis acid to synthesize $Ti_3C_2Cl_2$ MXene by molten salt etching. (*41*) Briefly, 1 g of pre-etch acid-washed excess metal-Ti_3AlC_2 MAX powder and 3 g of $ZnCl_2$ were added into a 50 mL centrifuge tube and kept for 30 minutes of rotary mixing. Then the mixed powders were transferred into an alumina crucible, then loaded to a quartz-tube furnace (Across International, USA) and heated to 650 °C at 3.5 °C/min under constant argon flow for 2 h. The etched multilayered $Ti_3C_2Cl_2$ MXene was then washed to remove unreacted $ZnCl_2$ with $\sim$30 mL of 12 M HCl for 6 h at room temperature. The acid-washed etched multilayered $Ti_3C_2Cl_2$ MXene was then neutralized using deionized water by repeated centrifugation in an Eppendorf centrifuge at 3234 RCF for 5 minutes. Then, the neutralized etched multilayered $Ti_3C_2Cl_2$ MXene solution was vacuum-filtered using a 0.22 μm filter membrane. The vacuum-filtered etched multilayered $Ti_3C_2Cl_2$ MXene powder was then dried under vacuum at room temperature for 24 h. The dried MXene powder was then transferred into the glovebox for delamination steps.

We used LiCl as an intercalant for the delamination of etched multilayered $Ti_3C_2Cl_2$ MXene. The delamination reaction was carried out in a 30 mL Nalgene high-density polyethylene bottle with a magnetic stir bar. For every 1 g of etched multilayered Ti3C2Cl2 MXene, 0.8 g LiCl was added to 20 mL DMSO (Sigma-Aldrich, >99.9%, anhydrous). Then, 1 g of etched multilayered $Ti_3C_2Cl_2$ MXene was added to the solution and stirred at 200 RPM for 24 h. The lithium intercalated $Ti_3C_2Cl_2$ MXene was then washed with ∼150 mL of DMSO for every 1 g of multilayered MXene powder by repeated centrifugation and decantation at 3234 RCF for 5 minutes in an Eppendorf centrifuge. After removing excess LiCl, the lithium intercalated $Ti_3C_2Cl_2$ MXene clay was redispersed in 20 mL of N-methylformamide (NMF, Sigma-Aldrich, >99.9%, anhydrous) for delamination and vortex mixed for 5 minutes. Then, NMF-dispersed $Ti_3C_2Cl_2$ MXene was washed by centrifugation and decantation at 3234 RCF for 5 minutes. After the NMF processing, swelling of the clay was observed. Then ∼20 mL of DMSO was added to the swelled MXene clay and vortex mixed for 15 minutes to isolate single-to-few MXene layers. Then, $Ti_3C_2Cl_2$ MXene colloidal suspension was processed by final centrifugation at 2380 RCF for 15 minutes. The supernatant containing single-to-few layered MXene was collected, and vacuum filtered using Celgard membrane to prepare MXene films.

Fabrication of MXene Films Monoflake films with thickness (∼ 1 nm) were spun-cast from the aqueous solution (1 mg/mL) on frosted glass (Fisherbran, Full-Frosted Cytology Microscope Slide) substrates. Multiflake films with thickness (∼ 60 nm) were drop-cast from the aqueous solution (10 mg/mL) on frosted glass. Multiflake films for vacuum annealing treatment were spun-cast from the aqueous solution (10 mg/mL) on Si wafers (500 ± 25 μm thick, p-type boron-doped, 0.01-0.05 ohm.cm, Virginia Semiconductor). The Si substrates (approximately 4 cm^2) were first cleaned with acetone, ethanol, and DI water. After drying with nitrogen gas, the substrates were exposed to oxygen plasma for 10 min. All colloidal solutions

were bath-sonicated for 2 min before spin-casting. Typically, films were constructed using a 100 μL solution via a two-step spin-casting (Laurell WS 400BZ-6NPP/Lite spin coater) process by spinning at 500 RPM for 60 s, followed by 2000 RPM for 10 s. For drop-casting, 100 μL solutions were added on the Si substrates and were left to dry in air either for 24 hours for aqueous solutions or for one week for DMSO solutions before measurement.

Vacuum Annealing Treatments For vacuum annealing treatment at 200 °C, MXene films were placed in an aluminum foil boat, then annealed in a vacuum oven (base pressure: $<$ 10 mTorr) for 24 h. For vacuum annealing at 600 °C, the samples were mounted onto a temperature-controlled Linkam stage (THMS600) inside a custom vacuum chamber (base pressure: 20-40 mTorr) and held for 2 h. The samples were then cooled to room temperature prior to other measurements.

Characterization Techniques

SEM Measurements Field-emission scanning electron microscopy (FESEM) was performed using a JEOL JSM-7800f FESEM with a lower electron detector at an acceleration voltage of 15 kV to study the MXene flake size and surface morphology. The solution concentration was maintained at $<$ 0.1 mg/mL and loaded on an anodic alumina disc, followed by vacuum drying for 2 h. The samples were gold sputtered to reduce the charging and improve the sharpness of SEM images.

EDS Measurements Energy dispersive X-ray spectroscopy (EDS) was conducted using an EDAX Octane Silicon Drift Detector in point scan mode with a 30 s exposure time. The EDS data was subsequently analyzed using the EDAX TEAM software.

AFM Imaging Atomic force microscopy (AFM) was carried out in tapping mode using a Bruker Icon AFM (Bruker, Santa Barbara, CA) instrument equipped with a closed-loop scanner. Tapping mode AFM Probes with Aluminum Reflective Coating (Budget Sensors, Tap300Al-G, resonance frequency ~ 300 kHz, tip radius ~ 10 nm) were used to record topography images in open-loop, with a 512×512 pixel resolution. AFM images were processed and analyzed using Gwyddion software. (*48*) A third-order polynomial was employed to flatten the background for topography images.

XRD Measurements X-ray diffraction (XRD) patterns of powder samples were analyzed using a Bruker D8 X-ray diffractometer with a Cu Kα (λ= 1.5406 Å) emitter and a VANTEC 500 detector. The powder samples were mounted on Kapton tapes and scanned from 5° to 80° with a step size of 5° and time per step of 30 seconds. The traditional XRD plots were obtained by merging and integrating the XRD^2 data in DIFFRAC. SUITE EVA software.

XPS Measurements X-ray photoelectron spectroscopy (XPS) measurements were performed using a PHI VersaProbe 5000 instrument (Physical Electronics) with a 200 μm and 50 W monochromatic Al-Kα (1486.6 eV) X-ray source. Charge neutralization was achieved by a dual-beam system involving low-energy Ar^+ ions and low-energy electrons at 1 eV and 200 μA. Survey spectra were collected with a pass energy of 117.4 eV and an energy resolution of 0.5 eV. More detailed analyses can be found in our previous work (*36*).

SE Measurements The spectroscopic ellipsometer (SE) used in this study was an M-2000 instrument (J.A. Woollam) with a wavelength range of 371 nm - 1687 nm (0.73 eV-3.34 eV). The SE beam size is 2 mm in diameter, representing that the measured film thickness is an ensemble-averaged value over a 4 mm^2 surface area of the sample. For optical property measurements, variable-angle measurements, at incident angles of 55°, 60°, 65°, 70°, and 75°, were performed

on these samples at room temperature. The SE results were modeled using the CompleteEase software (version 7.0) package. More details of the data modeling and results can be found in Supplementary Note S2, Figs.S7-8, and Tables S4-5, and our previous publications (*16, 36*).

UV-Vis absorption spectroscopy The absorption spectra of $Ti_3C_2T_x$ and $Ti_3C_2Cl_2$ MXene were collected using a Cary UV-Vis-NIR spectrophotometer with 1 cm quartz cuvettes over a range of 200 nm-1100 nm. The concentration of the $Ti_3C_2T_x$ and $Ti_3C_2Cl_2$ MXene was maintained at < 0.1 mg/ml. All spectra were recorded in DMSO, and DMSO was used as background for all measurements.

Electrical conductivity measurement For measuring the electrical conductivity, MXene films were prepared by vacuum-assisted filtration of single-to-few layered MXene colloidal suspension. Then the MXene films were annealed in vacuum at 200 °C for 24 hours. A four-point probe with a 1 mm separation connected to 2400 Keithley Source meter was employed to measure the film resistance. Using the thickness (d) from SEM images and sheet resistance (ρ_{ele}) from the four-point probe, the film's electrical conductivity (σ_{ele}) was calculated using the following equation:

$$\sigma_{\text{ele}} = \frac{1}{4.532 \times \rho_{\text{ele}} \times d} \tag{1}$$

SIMS Measurements The CAMECA IMS SC Ultra instrument was used for Secondary Ion Mass Spectrometry (SIMS) experiments. Cesium was used as a primary ion source. To reach the atomic depth resolution the measurement procedure was modified, which includes high incident angle bombardment (75°), ultra-low impact energy (100 eV), in-situ ion polishing, optimization of extraction parameters, super cycle, and advanced beam positioning, as described elsewhere (*34*). The SIMS profile results come from the bulk region of the free-standing MXene

films (at least 250 nm below the surface). The results were deconvoluted and calibrated according to the previously described protocol (*35*) and thus the exact composition of each atomic layer was determined.

DFT Calculations

Density functional theory (DFT) calculations were performed using the Vienna Ab initio Simulation Package (VASP) (*49, 50*). For all calculations, projector-augmented wave (PAW) pseudopotentials were used, where for Ti atoms, the valence 3d and semicore 4s electrons were included, and for C, O, and H atoms, only valence electrons were included. In order to capture the strong correction effects of Ti 3d electrons, DFT+U formalism was used. The effective U_{eff} value was determined by comparing the magnetic moments of monoflake Ti_3C_2 in DFT+U calculations and those in HSE06 calculations (*51*); the final value was chosen to be $U_{\text{eff}} = 3$ eV. For structural relaxation calculations, the force convergence criterion of 0.005 eV/Å and a vacuum of thickness of 20 Å was used (for monoflakes). The DFT-D3 correction scheme was used to capture the vdW interactions (*52*).

To calculate optical conductivity, we constructed tight-binding Hamiltonians based on maximally localized Wannier functions using the Wannier90 package (*53*). We chose the d-orbitals of Ti atoms, p-orbitals of C, O, F, and s-orbitals of H as the initial projections to construct the Wannier functions (for MXenes with different surface terminations). Using the constructed Wannier functions, we calculated the optical conductivity $\sigma^{\alpha\beta}_{\text{opt}}(\hbar\omega)$ and extinction coefficient $k^{\alpha\beta}(\hbar\omega)$ through

$$\sigma^{\alpha\beta}_{\text{opt}}(\hbar\omega) = \frac{2ie^2}{\hbar\omega}\sum_{m\neq n}\int \frac{d^3\mathbf{k}}{(2\pi)^3}\frac{v^{\alpha}_{mn}(\mathbf{k})v^{\beta}_{nm}(\mathbf{k})(f_{n\mathbf{k}} - f_{m\mathbf{k}})}{[\hbar\omega - (E_{n\mathbf{k}} - E_{m\mathbf{k}}) + i\hbar/\tau]} \tag{2}$$

$$k^{\alpha\beta}(\hbar\omega) = \text{Im}\sqrt{\frac{4\pi i}{\omega}\sigma^{\alpha\beta}(\omega)} \tag{3}$$

where $v^{\alpha}_{mn}(\mathbf{k})$ represents the velocity matrix element between bands m and n, $f_{n\mathbf{k}}$ is the Fermi-

Dirac occupation, and τ indicates the relaxation time.

When calculating the optical conductivity of monoflake $Ti_3C_2T_2$, the conductivity value was normalized according to $\sigma = \sigma_{\text{DFT}} \frac{z_{\text{cell}}}{z_{\text{monoflake}}}$, so that the calculated conductivity does not depend on the vacuum thickness. The same procedure was also applied to the calculated plasmon frequency, as described below.

Surface plasmon waves. To study the surface plasmon effect, the total dielectric function was split into the inter-band contributions and the intraband contributions,

$$\varepsilon_{r,\text{inter}} = \frac{i}{\omega}\sigma_{\text{opt}} \tag{4}$$

$$\varepsilon_{r,\text{intra}} = 1 - \frac{\omega_p^2}{\omega^2 + i\omega\eta} \tag{5}$$

The inter-band dielectric function was directly converted from the (complex inter-band) optical conductivity σ_{opt} from the Wannier90 package (*53*) (with the smearing width 0.05 eV), while the intraband dielectric function was calculated from a Drude model, where the plasmon frequency ω_p was calculated using the VASP package (*49, 50*), and η was also set to be 0.05 eV. We combine the two contributions together and obtain the total dielectric function $\varepsilon_r(\omega) = \varepsilon_{r,\text{inter}} + \varepsilon_{r,\text{intra}}$, from which the dispersion relation of the surface plasmon mode was calculated as

$$\beta = \frac{\omega}{c}\sqrt{\frac{\varepsilon_r}{\varepsilon_r + 1}} \tag{6}$$

where β is the in-plane wave vector of surface waves, c is the speed of light, and we chose the vacuum as the dielectric medium (*54*).

To calculate the experimental surface plasmon modes shown in Fig.s 2C&D, Equation 6 was used along with experimentally measured dielectric constants shown in Figs. 2A&B. A vacuum normalization procedure used in optical conductivity calculations was also applied to the to the calculated plasmon frequency.

SUPPLEMENTARY MATERIALS

REFERENCES AND NOTES

1. M. Naguib, M. Kurtoglu, V. Presser, J. Lu, J. Niu, M. Heon, L. Hultman, Y. Gogotsi, M. W. Barsoum, Two-dimensional nanocrystals produced by exfoliation of Ti_3AlC_2. *Advanced Materials* **23**, 4248–4253 (2011).

2. A. VahidMohammadi, J. Rosen, Y. Gogotsi, The world of two-dimensional carbides and

nitrides (MXenes). *Science* **372**, eabf1581 (2021).

3. K. Hantanasirisakul, M.-Q. Zhao, P. Urbankowski, J. Halim, B. Anasori, S. Kota, C. E. Ren, M. W. Barsoum, Y. Gogotsi, Fabrication of $Ti_3C_2T_x$ MXene transparent thin films with tunable optoelectronic properties. *Advanced Electronic Materials* **2**, 1600050 (2016).

4. B. Lyu, M. Kim, H. Jing, J. Kang, C. Qian, S. Lee, J. H. Cho, Large-area MXene electrode array for flexible electronics. *ACS Nano* **13**, 11392–11400 (2019).

5. K. Hantanasirisakul, Y. Gogotsi, Electronic and optical properties of 2d transition metal carbides and nitrides (mxenes). *Advanced Materials* **30**, 1804779 (2018).

6. Y. Gogotsi, B. Anasori, The rise of MXenes. *ACS Nano* **13**, 8491–8494 (2019).

7. M. Naguib, M. W. Barsoum, Y. Gogotsi, Ten years of progress in the synthesis and development of mxenes. *Advanced Materials* **33**, 2103393 (2021).

8. Y. Gogotsi, The future of mxenes. *Chemistry of Materials* **35**, 8767-8770 (2023).

9. X. Li, Z. Huang, C. E. Shuck, G. Liang, Y. Gogotsi, C. Zhi, MXene chemistry, electrochemistry and energy storage applications. *Nature Reviews Chemistry* **6**, 389–404 (2022).

10. B. Anasori, M. R. Lukatskaya, Y. Gogotsi, 2D metal carbides and nitrides (MXenes) for energy storage. *Nature Reviews Materials* **2**, 1–17 (2017).

11. L. R. Johnson, S. Sridhar, L. Zhang, K. D. Fredrickson, A. S. Raman, J. Jang, C. Leach, A. Padmanabhan, C. C. Price, N. C. Frey, *et al.*, Mxene materials for the electrochemical nitrogen reduction—functionalized or not? *ACS Catalysis* **10**, 253–264 (2019).

12. A. Miranda, J. Halim, M. Barsoum, A. Lorke, Electronic properties of freestanding $Ti_3C_2T_x$ mxene monolayers. *Applied Physics Letters* **108**, 033102 (2016).

13. K. Maleski, C. E. Shuck, A. T. Fafarman, Y. Gogotsi, The broad chromatic range of two-dimensional transition metal carbides. *Advanced Optical Materials* **9**, 2001563 (2021).

14. X. Xu, T. Guo, M. Lanza, H. N. Alshareef, Status and prospects of mxene-based nanoelectronic devices. *Matter* **6**, 800–837 (2023).

15. V. Mauchamp, M. Bugnet, E. P. Bellido, G. A. Botton, P. Moreau, D. Magne, M. Naguib, T. Cabioc'h, M. W. Barsoum, Enhanced and tunable surface plasmons in two-dimensional ti 3 c 2 stacks: Electronic structure versus boundary effects. *Physical Review B* **89**, 235428 (2014).

16. A. A. Shamsabadi, H. Fang, D. Zhang, A. Thakur, C. Y. Chen, A. Zhang, H. Wang, B. Anasori, M. Soroush, Y. Gogotsi, Z. Fakhraai, The evolution of mxenes conductivity and optical properties upon heating in air. *Small Methods* **7**, 2300568 (2023).

17. C. Raab, J. Rieger, A. Ghosh, J. L. Spellberg, S. B. King, Surface plasmons in two-dimensional mxenes. *The Journal of Physical Chemistry Letters* **15**, 11643–11656 (2024).

18. H. Lashgari, M. Abolhassani, A. Boochani, S. Elahi, J. Khodadadi, Electronic and optical properties of 2d graphene-like compounds titanium carbides and nitrides: Dft calculations. *Solid State Communications* **195**, 61–69 (2014).

19. M. Khazaei, M. Arai, T. Sasaki, A. Ranjbar, Y. Liang, S. Yunoki, OH-terminated two-dimensional transition metal carbides and nitrides as ultralow work function materials. *Physical Review B* **92**, 075411 (2015).

20. E. C. Glor, R. C. Ferrier, C. Li, R. J. Composto, Z. Fakhraai, Out-of-plane orientation alignment and reorientation dynamics of gold nanorods in polymer nanocomposite films. *Soft Matter* **13**, 2207–2215 (2017).

21. C. Gao, Z. Lu, Y. Liu, Q. Zhang, M. Chi, Q. Cheng, Y. Yin, Highly stable silver nanoplates for surface plasmon resonance biosensing. *Angewandte Chemie* **124**, 5727–5731 (2012).

22. H. Fang, M. J. Wilhelm, J. Ma, Y. Rao, D. L. Kuhn, Z. Zander, B. G. DeLacy, H.-L. Dai, Ag nanoplatelets as efficient photosensitizers for TiO_2 nanorods. *The Journal of Chemical Physics* **156** (2022).

23. K. Maleski, C. E. Ren, M.-Q. Zhao, B. Anasori, Y. Gogotsi, Size-dependent physical and electrochemical properties of two-dimensional mxene flakes. *ACS Applied Materials & Interfaces* **10**, 24491–24498 (2018).

24. K. Maleski, V. N. Mochalin, Y. Gogotsi, Dispersions of two-dimensional titanium carbide mxene in organic solvents. *Chemistry of Materials* **29**, 1632–1640 (2017).

25. J. K. El-Demellawi, S. Lopatin, J. Yin, O. F. Mohammed, H. N. Alshareef, Tunable multipolar surface plasmons in 2d $Ti_3C_2T_x$ mxene flakes. *ACS Nano* **12**, 8485–8493 (2018).

26. D. B. Lioi, P. R. Stevenson, B. T. Seymour, G. Neher, R. D. Schaller, D. J. Gosztola, R. A. Vaia, J. P. Vernon, W. J. Kennedy, Simultaneous ultrafast transmission and reflection of nanometer-thick $Ti_3C_2T_x$ mxene films in the visible and near-infrared: Implications for energy storage, electromagnetic shielding, and laser systems. *ACS Applied Nano Materials* **3**, 9604–9609 (2020).

27. P. Salles, D. Pinto, K. Hantanasirisakul, K. Maleski, C. E. Shuck, Y. Gogotsi, Electrochromic effect in titanium carbide MXene thin films produced by dip-coating. *Advanced Functional Materials* **29**, 1809223 (2019).

28. J. Rieger, A. Ghosh, J. Spellberg, C. Raab, A. Mohan, P. Joshi, S. King, Imaging and simulation of surface plasmon polaritons on layered 2D mxenes. *ChemRxiv* pp. https://chemrxiv.org/engage/chemrxiv/article–details/66ba644a5101a2ffa81dc23b (2024).

29. X. Guo, N. Li, C. Wu, X. Dai, R. Qi, T. Qiao, T. Su, D. Lei, N. Liu, J. Du, *et al.*, Studying plasmon dispersion of mxene for enhanced electromagnetic absorption. *Advanced Materials* **34**, 2201120 (2022).

30. A. Furchner, T. Parker, V. Mauchamp, S. Hurand, J. Plaickner, J. Rappich, A. A. Emerenciano, K. Hinrichs, Y. Gogotsi, T. Petit, $Ti_3C_2T_x$ mxene thin films and intercalated species characterized by ir-to-uv broadband ellipsometry. *ChemRxiv* pp. https://chemrxiv.org/engage/chemrxiv/article–details/6710e769cec5d6c14268a400 (2024).

31. D. A. Panova, G. I. Tselikov, G. A. Ermolaev, A. V. Syuy, D. S. Zimbovskii, O. O. Kapitanova, D. I. Yakubovsky, A. B. Mazitov, I. A. Kruglov, A. A. Vyshnevyy, *et al.*, Broadband optical properties of Ti_3C_2 mxene revisited. *Optics Letters* **49**, 25–28 (2023).

32. N. Liu, Q. Li, H. Wan, L. Chang, H. Wang, J. Fang, T. Ding, Q. Wen, L. Zhou, X. Xiao, High-temperature stability in air of $Ti_3C_2T_x$ MXene-based composite with extracted bentonite. *Nature Communications* **13**, 1–10 (2022).

33. M. Li, J. Lu, K. Luo, Y. Li, K. Chang, K. Chen, J. Zhou, J. Rosen, L. Hultman, P. Eklund, *et al.*, Element replacement approach by reaction with lewis acidic molten salts to synthesize nanolaminated max phases and mxenes. *Journal of the American Chemical Society* **141**, 4730–4737 (2019).

34. P. P. Michaĺowski, M. Anayee, T. S. Mathis, S. Kozdra, A. Wójcik, K. Hantanasirisakul, I. Jóźwik, A. Piatkowska, M. Możdżonek, A. Malinowska, *et al.*, Oxycarbide mxenes and max phases identification using monoatomic layer-by-layer analysis with ultralow-energy secondary-ion mass spectrometry. *Nature Nanotechnology* **17**, 1192–1197 (2022).

35. P. P. Michaĺowski, Unraveling the composition of each atomic layer in the mxene/max phase structure–identification of oxycarbide, oxynitride, and oxycarbonitride subfamilies of mxenes. *Nanoscale Horizons* **9**, 1493–1497 (2024).

36. H. Fang, A. Thakur, A. Zahmatkeshsaredorahi, Z. Fang, V. Rad, A. Shamsabadi, Ahmad, C. Pereyra, M. Soroush, M. A. Rappe, G. X. Xu, B. Anasori, Z. Fakhraai, Stabilizing $Ti_3C_2T_x$ mxene flakes in air by removing confined water. *Proceedings of the National Academy of Sciences* **121**, e2400084121 (2024).

37. A. D. Dillon, M. J. Ghidiu, A. L. Krick, J. Griggs, S. J. May, Y. Gogotsi, M. W. Barsoum, A. T. Fafarman, Highly conductive optical quality solution-processed films of 2D titanium carbide. *Advanced Functional Materials* **26**, 4162–4168 (2016).

38. K. Chaudhuri, M. Alhabeb, Z. Wang, V. M. Shalaev, Y. Gogotsi, A. Boltasseva, Highly broadband absorber using plasmonic titanium carbide (mxene). *ACS Photonics* **5**, 1115–1122 (2018).

39. S. L. Murray, S. Serajian, S. I. Gnani Peer Mohamed, S. Robinson, R. Krishnamoorthy, S. R. Das, M. Bavarian, S. Nejati, U. Kilic, M. Schubert, *et al.*, Ultrabroadband optical properties of 2D Titanium Carbide Mxene. *ACS Applied Materials & Interfaces* (2024).

40. A. Thakur, N. Chandran B.S., K. Davidson, A. Bedford, H. Fang, Y. Im, V. Kanduri, B. C. Wyatt, S. K. Nemani, V. Poliukhova, R. Kumar, Z. Fakhraai, B. Anasori, Step-by-step guide for synthesis and delamination of $Ti_3C_2T_x$ MXene. *Small Methods* **7**, 2300030 (2023).

41. T. Zhang, K. Shevchuk, R. J. Wang, H. Kim, J. Hourani, Y. Gogotsi, Delamination of chlorine-terminated mxene produced using molten salt etching. *Chemistry of Materials* **36**, 1998–2006 (2024).

42. T. Hu, Z. Li, M. Hu, J. Wang, Q. Hu, Q. Li, X. Wang, Chemical origin of termination-functionalized MXenes: $Ti_3C_2T_2$ as a case study. *The Journal of Physical Chemistry C* **121**, 19254–19261 (2017).

43. G. Berdiyorov, Optical properties of functionalized $Ti_3C_2T_2$ (T= F, O, OH) mxene: First-principles calculations. *AIP Advances* **6**, 055105 (2016).

44. A. Archambault, T. V. Teperik, F. Marquier, J.-J. Greffet, Surface plasmon fourier optics. *Physical Review B—Condensed Matter and Materials Physics* **79**, 195414 (2009).

45. K. D. Fredrickson, B. Anasori, Z. W. Seh, Y. Gogotsi, A. Vojvodic, Effects of applied potential and water intercalation on the surface chemistry of Ti_2C and Mo_2C mxenes. *The Journal of Physical Chemistry C* **120**, 28432–28440 (2016).

46. J. H. Mokkath, Photo-response of water intercalated $Ti_3C_2O_2$ mxene. *Physical Chemistry Chemical Physics* **25**, 9522–9531 (2023).

47. T. S. Mathis, K. Maleski, A. Goad, A. Sarycheva, M. Anayee, A. C. Foucher, K. Hantanasirisakul, C. E. Shuck, E. A. Stach, Y. Gogotsi, Modified MAX phase synthesis for environmentally stable and highly conductive Ti_3C_2 MXene. *ACS Nano* **15**, 6420–6429 (2021).

48. D. Nečas, P. Klapetek, Gwyddion: an open-source software for spm data analysis. *Open Physics* **10**, 181–188 (2012).

49. G. Kresse, J. Hafner, Ab initio molecular dynamics for liquid metals. *Physical Review B* **47**, 558 (1993).

50. G. Kresse, J. Furthmüller, Efficient iterative schemes for ab initio total-energy calculations using a plane-wave basis set. *Physical Review B* **54**, 11169 (1996).

51. M. E. Jochen Heyd, Gustavo E. Scuseria, Hybrid functionals based on a screened coulomb potential. *J. Chem. Phys.* **118**, 8207-8215 (2003).

52. L. G. Stefan Grimme, Stephan Ehrlich, Effect of the damping function in dispersion correcteddensity functional theory. *Journal of Computational Chemistry* **32**, 1456-1465 (2011).

53. A. A. Mostofi, J. R. Yates, G. Pizzi, Y.-S. Lee, I. Souza, D. Vanderbilt, N. Marzari, An updated version of wannier90: A tool for obtaining maximally-localised wannier functions. *Computer Physics Communications* **185**, 2309-2310 (2014).

54. S. Guan, S. A. Yang, L. Zhu, J. Hu, Y. Yao, Electronic, dielectric, and plasmonic properties of two-dimensional electride materials X_2N (x=Ca, Sr): A first-principles study. *Scientific Reports* **5**, 12285-12285 (2015).

Acknowledgement: The authors acknowledge Dr. Lianne Beltran for professional editing. Za.F. and H.F. thank Prof. Alexandra Vojvodic for her helpful insight and discussions. H.F. acknowledges the School of Arts and Sciences at the University of Pennsylvania for the Post-doctoral Fellowship. **Funding:** The authors acknowledge funding support from the US National Science Foundation, award number CMMI-2134607. Zh.F. acknowledges funding from the US National Science Foundation, award number CHE-2303044. P.P.M. was supported by the National Center for Research and Development (Project No. LIDER/8/0055/L-12/20/NCBR/2021).
Author contributions: H.F. and Za.F. conceived the experiments; H.F. conducted SE and AFM characterization, performed data analysis, prepared the first draft of the manuscript; Zh.F. performed theoretical calculations and wrote the paper under the supervision of A.M.R.; A.T. and N.C. conducted the material synthesis, XRD, SEM, EDS, UV-vis and electric conductivity characterizations under the supervision of B.A.; V.R. conducted XPS characterization under the

supervision of M.S.; P.P.M conducted SIMS experiments; B.A., A.M.R., and Za.F. supervised the studies. The manuscript was written through contributions from all authors, and all authors have given approval to the final version of the manuscript. **Competing interests:** We declare no such interests. **Data and materials availability:** All data needed to evaluate the conclusions in the paper are present in the paper and supplementary materials.